Geophysical Research Letters

RESEARCH LETTER
10.1029/2019GL082493

# Melting at the Edge of a Slab in the Deepest Mantle

**Michael S. Thorne[1], Nozomu Takeuchi[2], and Katsuhiko Shiomi[3]**

[1]Department of Geology and Geophysics, University of Utah, Salt Lake City, UT, USA, [2]Earthquake Research Institute, University of Tokyo, Tokyo, Japan, [3]National Research Institute for Earth Science and Disaster Resilience, Tsukuba, Japan

**Key Points:**
- Subducted slab material resting on the core-mantle boundary is ringed by ultralow-velocity zones
- A partially molten origin to these ultralow-velocity zones is likely
- Melting of mid-ocean ridge basalt may give rise to ultralow-velocity zones

**Supporting Information:**
- Supporting Information S1
- Data Set S1
- Movie S1

**Correspondence to:**
M. S. Thorne,
michael.thorne@utah.edu

**Citation:**
Thorne, M. S., Takeuchi, N., & Shiomi, K. (2019). Melting at the edge of a slab in the deepest mantle. *Geophysical Research Letters*, *46*, 8000–8008. https://doi.org/10.1029/2019GL082493

Received 20 FEB 2019
Accepted 24 JUN 2019
Accepted article online 3 JUL 2019
Published online 24 JUL 2019



**Abstract** We analyzed new recordings of *SPdKS* seismic waveforms from a global set of broadband seismograms and horizontal tiltmeters from the Hi-net array in Japan from 26 earthquakes in the Central American region. The anomalous waveforms are consistent with the presence of at least three ultralow-velocity zones (ULVZs), on the core-mantle boundary beneath northern Mexico and the southeastern United States. These ULVZs ring an area of high seismic wave speeds observed in tomographic models that has long been associated with past subduction. Waveform modeling using the PSVaxi method suggests that the ULVZs have *S* and *P* wave velocity decreases of 40% and 10%, respectively. These velocity decreases are likely best explained by a partially molten origin where the melt is generated through melting of mid-ocean ridge basalt atop the subducted slab.

**Plain Language Summary** We use a set of seismic observations recorded globally to investigate the lower mantle beneath Central America. The deepest mantle in this region has been associated with the final resting place of subducted slab material from subduction that initiated approximately 200 million years ago. This ancient subducted material is associated with high seismic wave speeds in the lowermost mantle just above the core-mantle boundary. We find that patches of highly reduced seismic wave speeds, referred to as ultralow-velocity zones (ULVZs), appear to be associated with the border of the high wave speed region, along the border of the subducted slab material. These ULVZ patches are consistent with being regions of partial melt. A possible scenario for their creation is that mid-ocean ridge basalt (MORB), comprising the crust of the subducted slab material, has a low melting point at conditions in the deep earth and may be melting as the slabs reach the bottom of the mantle. Previous experimental work has suggested that MORB will likely partially melt in the deep mantle, yet little evidence for the existence of MORB partial melt has previously been found.

## 1. Introduction

Enigmatic zones of ultra reduced wave speeds sitting directly on top of the core-mantle boundary (CMB), referred to as ultralow-velocity zones (ULVZs), were first discovered in the early 1990s (Garnero et al., 1993). A variety of mechanisms have been proposed to explain ULVZ origins (Li et al., 2017), but the most commonly invoked hypothesis remains a partial melt origin (Berryman, 2000; Williams & Garnero, 1996). Several studies have shown that data are consistent with the expected 3:1 ratio between *S* wave and *P* wave velocity reductions ($\delta V_S/\delta V3$) for a partially molten ULVZ (Helmberger et al., 2000; Reasoner & Revenaugh, 2000; Thorne et al., 2013). However, trade-offs exist between ULVZ elastic parameters and morphology (Garnero & Helmberger, 1998) and the waveforms can commonly be fit by models with a 1:1 or 2:1 $\delta V_S/\delta V_P$ ratio, consistent with a compositional origin (Brown et al., 2015).

Not everything reported as ULVZs may be a manifestation of the same thing. Wave speed reductions as large as 45% for *S* waves (Thorne et al., 2013) and 23% for *P* waves (Brown et al., 2015) have been reported. In contrast, wave speed reductions as low as 3% for *S* waves (Avants et al., 2006) and 2% for *P* waves (Hutko et al., 2009) have been indicated. ULVZ elastic parameters described span this entire range (Bower et al., 2011; Yu & Garnero, 2018). This wide variety of properties could be a result of trade-offs in the model space but may indicate that ULVZs are heterogeneous in their properties, undergo time-varying changes in properties, or that we are lumping all features with low seismic velocities into the same class of object.

Insight into ULVZ origins may be gained by constraining their location on the CMB. An initial effort linked ULVZs to hot spot volcanism (Williams et al., 1998). Several ULVZs have been detected beneath hot spots such as Hawaii (Cottaar & Romanowicz, 2012), Comores (Wen, 2000), Samoa (Thorne et al., 2013), and Iceland (Helmberger et al., 1998; Yuan & Romanowicz, 2017). Recent tomographic efforts have also linked

whole mantle plumes rooted in ULVZs to hot spots (French & Romanowicz, 2015). Geodynamic efforts have suggested that dense compositionally distinct ULVZs should cluster near the edges of large low shear velocity provinces (LLSVPs; Li et al., 2017; McNamara et al., 2010). This prediction has been preliminarily corroborated (Yu & Garnero, 2018). The edges of LLSVPs may in turn be linked to the formation of whole mantle plumes (*Boschi* et al., 2007; Thorne et al., 2004; Torsvik et al., 2006), and thus, hot spot volcanism may also be linked to compositional ULVZs. Yet, only a small percentage of the CMB has been searched for ULVZs and a clearer picture may emerge as more of the CMB has been mapped.

There is a large amount of uncertainty in temperature at the CMB (Anzellini et al., 2013; Zhang et al., 2016), but, of the possible lower mantle constituents, subducted mid-ocean ridge basalt (MORB), is predicted to have the lowest melting temperature (Andrault et al., 2014; Pradhan et al., 2015). As the D″ region may be the final resting place of subducted slabs (Fukao et al., 2001; Grand et al., 1997), partial melting of MORB has been suggested as a source of partially molten ULVZs. Yet, only a couple of ULVZs have been detected at locations where we infer recent subduction (Havens & Revenaugh, 2001; Niu & Wen, 2001).

Here we present evidence for partially molten ULVZs at the edges of a subducted slab beneath Central America. The locations of these ULVZs tend to ring the region dominated by high seismic wave speeds in tomographic models (e.g., Houser et al., 2008; Ritsema et al., 2011; Takeuchi, 2007). This region has routinely been identified as the remnants of subduction beginning roughly 200 Ma to the west of North and Central America (Grand, 2002; Sigloch & Mihalynuk, 2013).

## 2. Seismic Data and Data Processing

We focus on waveforms in the time window around the *SPdKS* seismic phase (Figure 1a). This phase is composed of $P_{diff}$ arcs along the CMB starting where either the downgoing *S* wave hits the CMB at the critical distance to initiate source-side *P* wave diffraction (*SPdKS*), or an upgoing *SKS* wave in the outer core hits the CMB at the critical distance to initiate receiver-side *P* wave diffraction (*SKPdS*). What is referred to as *SPdKS* is a combination of pure *SPdKS* (dark blue ray in Figure 1a), pure *SKPdS* (dark orange ray in Figure 1a), and combinations of these two end member scenarios (other colored rays in Figure 1a).

We searched for earthquakes in Central America (latitudes of 5°N to 20°N and longitudes 75°W to 105°W) with magnitudes ≥5.7 and depths ≥75 km occurring between 1990 and 2015. We collected recordings from a global search for three-component broadband stations, and horizontal tiltmeter recordings in Japan (Table S1 in the supporting information).

We collected data for broadband stations within the epicentral distance range from 90° to 125°. Broadband recordings are collected from the Incorporated Research Institutions for Seismology (IRIS), the Observatories and Research Facilities for European Seismology, and the Full Range Seismograph Network of Japan (F-net). Data processing steps included (1) removing the mean and trends, (2) removing the instrument response, (3) band-pass filtering between 0.01 and 1 Hz, and (4) rotating to radial component. We inspected each trace and retained seismograms that showed clear *SKS* energy, using the identification of *SKKS*, *SPdKS*, *sSKS*, and $SV_{diff}$ as indicators of proper phase identification and polarity.

Data for each event was inspected at the F-net stations in order to determine which events showed the cleanest *SKS* energy recorded in Japan. We collected additional recordings of horizontal tiltmeter sensors for five high-quality events (Table S1) from the High Sensitivity Seismograph Network Japan (Hi-net) operated by the National Research Institute for Earth Science and Disaster Resilience (NIED), Japan. The NIED operates tiltmeters at over 700 sites (Figure 2a). Tiltmeter recordings have been used as seismic recordings in previous studies (Takeuchi & Obara, 2010; Tonegawa et al., 2006). Tiltmeter recordings are provided as tilt angle measured in radians and can be converted to horizontal accelerations by multiplying by $-g$, where $g$ is gravitational acceleration. The high degree of similarity between broadband seismograph recordings and tiltmeter recordings is shown in Figure 2b. Tiltmeter recordings were also inspected for quality similar to broadband recordings. We retained high-quality recordings from 3,588 broadbands and 2,405 tiltmeters for a total of 5,993 recordings.

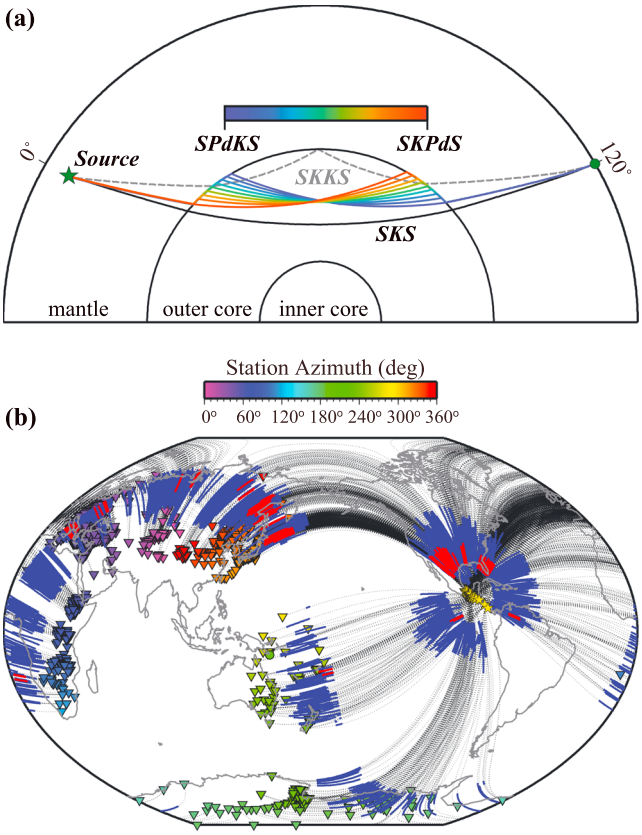


**Figure 1.** (a) Raypaths are drawn for *SKS* (black) and range from pure *SPdKS* (blue) to pure *SKPdS* (orange). Raypaths are drawn for a 500-km event depth at an epicentral distance of 120°. (b) Earthquake locations are drawn with red stars and receivers are drawn as triangles. The Pd segment on the CMB of *SPdKS* are drawn with blue (normal) or red (anomalous) lines.

## 3. Anomalous Seismic Waveforms

We inspected *SPdKS* waveforms for events occurring in the Central American region recorded globally (Figure 1b). Multiple events show an apparent *SPdKS* arrival emerging at an epicentral distance of approximately 112° with a larger amplitude than the *SKS* arrival, which does not occur for a PREM background velocity. Previous studies have linked this waveform complexity to ULVZ presence (Ni & Helmberger, 2001; Thorne et al., 2013; Wen & Helmberger, 1998). Further waveform complexity exists at distances from approximately 108° to 112°, in which up to three arrivals are apparent. We classify all seismic arrivals in the distance range $108° \geq \Delta \geq 114°$ as anomalous if they either (1) show an apparent *SPdKS* arrival with larger amplitude than *SKS* or (2) show multiple arrivals in the 108° to 112° distance range. Anomalous waveforms are classified using an automatic peak finding algorithm. Peaks are considered if they are greater than 80% the amplitude of the largest arrival in the *SKS* time window. Anomalous waveforms are manually verified using the $3\pi/2$ phase-shifted *SKKS* arrival overlain on the anomalous trace to ensure that the waveform complexity only occurs in the vicinity of the *SKS* arrival (inset in Figure 3).

Locations of anomalous waveforms are shown in Figure 1b (red $P_{diff}$ segments) and in Figure 3, where in Figure 3 only the point where CMB *P* diffraction initiates is plotted. Distance profiles for all events and anomalous waveforms are provided in the supporting information. Anomalous waveforms cluster into five groups around the boundary of the highest *S* wave speeds. We have labeled two areas as potential ULVZs. Waveforms in these regions display ULVZ signatures. But, for these anomalies, the Pd portion of *SPdKS* and *SKPdS* are tightly clustered on both source and receiver sides of the raypath. Furthermore, the receiver-side Pd segments occur at the western edge of Africa and the western Pacific region where previous evidence has been shown for ULVZs (Idehara et al., 2007; Jensen et al., 2013; *Rost* et al., 2010). The area to the west of Africa has not been explored (Yu & Garnero, 2018) but is within the African LLSVP and may contain ULVZs. Hence, both locations are labeled as potential ULVZs as ULVZ structure is equally likely to occur on the receiver side.

Three clusters of anomalous waveforms exist on the northern boundary of the fast wave speed region. The clusters are centered at (1) northern Mexico (~27°N, 101°W), (2) south of Louisiana (~29°N, 92.5°W), and (3) west of Florida (~25°N, 84°W). These ULVZs likely exist on the source side (*SPdKS*) of the raypath for the following reasons. First, the northern Mexico ULVZ partially overlaps ULVZ structure identified using *PcP* reflections (Havens & Revenaugh, 2001; region outlined in Figure 3) and noise correlations of ScS (Spica et al., 2017; Figure S1). Second, anomalous waveforms showing a high degree of similarity in waveform shape are recorded at widely separated receivers but have closely located Pd paths on the source side. Third, for the Florida ULVZ, there exists crossing coverage of source-side Pd arcs with anomalous waveforms. In addition, receiver-side Pd arcs from South Sandwich Island events that cross the Florida ULVZ also display similarly anomalous waveforms (Figures S25–S27).

## 4. Waveform Modeling

We use the axisymmetric finite difference code PSVaxi (Jahnke, 2009) to model seismic waveforms. The PSVaxi technique has been used in multiple studies of deep mantle heterogeneity (e.g., Jensen et al., 2013; Thorne et al., 2013). Computations are carried out on a 2-D grid and rotated virtually in 3-D about the axis passing through the center of the Earth and the earthquake source, thus retaining correct 3-D geometrical spreading, albeit for a 2-D model.

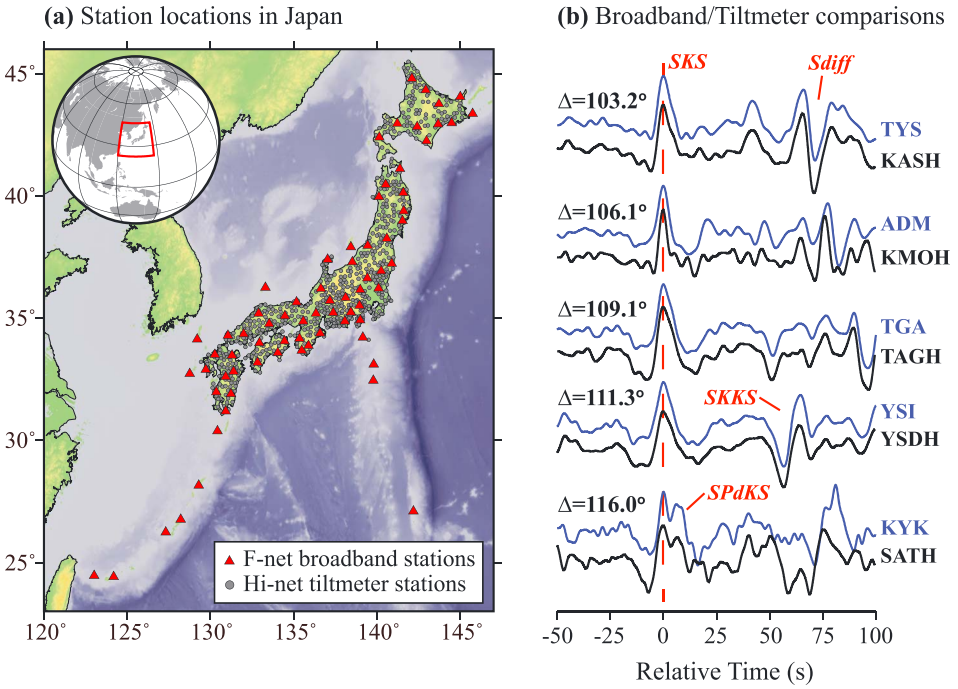


**Figure 2.** (a) The locations of F-net broadband sensors are drawn with red triangles and the Hi-net tiltmeter stations are drawn with gray circles. (b) Comparison of F-net broadband recordings (blue traces) with Hi-net tiltmeter recordings (black traces). Shown are radial component displacement traces aligned and normalized to unity on the *SKS* arrival. All records are band-pass filtered with corners between 0.02 and 0.2 Hz. Records are shown for the 25 February 2011 event.

Anomalous *SPdKS* waveforms similar to those observed in this study have previously been interpreted and modeled with ULVZ structures on the CMB (Ni & Helmberger, 2001; Thorne et al., 2013; Wen & Helmberger, 1998). Using the PSVaxi technique, we compute synthetic seismograms where we alter the ULVZ elastic parameters: (1) *S* wave velocity reduction ($\delta V_S$), (2) *P* wave velocity reduction ($\delta V_P$), and (3) density ($\rho$). We also alter the ULVZs dimensions and location by modifying (4) the ULVZ thickness ($h$), the length of the ULVZ along the great circle path (*length*), and the angular distance from the source where the boundary, or edge, of the ULVZ is first encountered ($l_1$). We computed synthetic seismograms for over 1,500 unique models. Synthetics were not computed in a strict parameter grid space, but parameters in the following range were explored: $\delta V_S$: −55% to −10%; $\delta V_P$: −50% to −5%; $h$: 5 to 45 km, length: 1° to 26°, $l_1$: 2° to 25°. All synthetics were computed for a 100-km source depth and a dominant period of 6 s with a density of +10% relative to the PREM model (Dziewonski & Anderson, 1981).

For each event we constructed distance profiles to compare with synthetic seismograms. Distance profiles are created by aligning seismic traces on the PREM-predicted *SKS* arrival. Data are stacked in 1° epicentral distance bins. Seismic traces analyzed in this study were recorded for event depths ranging from 80 to 211 km. To reduce the numbers of synthetic seismograms we needed to compute, we shifted the epicentral distance of each recording to a source depth of 100 km using the following formula:

$$\Delta_S = (0.002°/\mathrm{km})\left(EV_{\mathrm{depth}} - CS_{\mathrm{depth}}\right) + \Delta \quad (1)$$

where $\Delta$ is the original event-receiver distance, $\Delta_S$ is the shifted distance, $EV_{\mathrm{depth}}$ is the event depth, and $CS_{\mathrm{depth}}$ is common source depth to shift the seismograms by.

We compare events to synthetic models by calculating the root-mean-square (RMS) misfit between data stack, $s_{\mathrm{data}}$, and nearest distance synthetic, $s_{\mathrm{ULVZ}}$. The calculation is done in a 25-s window starting 5 s before the *SKS* arrival, where both data stack and synthetic are normalized to the maximum amplitude within the time window. We obtain a single measure for goodness of fit of the model by averaging each RMS misfit calculation for each of the $N$ data stacks in the event:

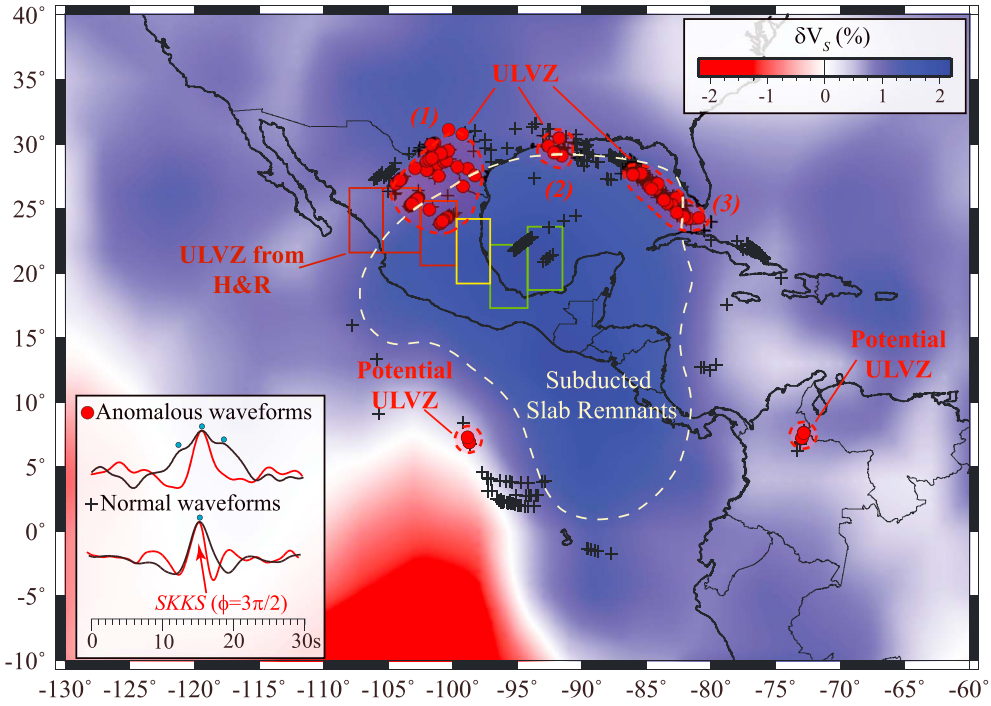


**Figure 3.** Waveforms are characterized as anomalous with Pd-inception point on the CMB mapped as a red circle or as normal with inception point mapped as a black cross. The inset shows example anomalous (upper) and normal (lower) *SKS* waveforms in black, with the equivalent 3π/2 phase shifted *SKKS* arrival overlain in red for comparison. Anomalous traces show multiple arrivals, as indicated with the blue dots. The background *S* wave velocity model is GyPSuM (Simmons et al., 2010). ULVZs detected in this study are outlined with red dashed lines. Red boxes show ULVZ detection from the study of Havens and Revenaugh (2001). The neighboring yellow and green boxes shows regions from the same study that respectively indicate a possibly large ULVZ and no ULVZ. ULVZ = ultralow-velocity zone.

$$Misfit = \frac{1}{N}\sum_{i=1}^{N}\sqrt{\frac{\sum_{t=-5}^{20}|s_{\mathrm{ULVZ}}(t)-s_{\mathrm{data}}(t)|^2}{\sum_{t=-5}^{20}|s_{\mathrm{data}}(t)|^2}} \quad (2)$$

Events recorded at the Hi-net array provide unique distance profiles for which we can compare synthetic seismograms. In particular, four events provide overlapping coverage of the northern Mexico ULVZ (Figure S44). Figures 4a and 4c show two of the most distinctive events. These waveforms are characterized by the emergence of three distinct arrivals at approximately 112°, which are persistent out to distances of 118°. The second arrival emerges with an amplitude that is larger than the first arrival. At a distance of about 115° the first arrival becomes the largest amplitude arrival.

Model misfit is shown for the four events that sample the northern Mexico ULVZ in Figures 4e–4h. In this plot model misfit is arranged as a function of $\delta V_S$ and $\delta V_P$. Because a single combination of $\delta V_S$ and $\delta V_P$ may be represented by multiple models (e.g., different thicknesses or lengths), we only show the result for the model with the lowest misfit. Symbol size and color represent the degree of misfit, where larger circles represent models that fit these data best. A range of possible velocity contrasts appears acceptable in these plots, but models with $\delta V_S$ near −40% and $\delta V_P$ near −10% fit the waveforms for all four events. Only a handful of models computed reproduce the unique waveform characteristics shown in Figures 4a and 4c. Model misfits are also low for $\delta V_S$ near −15% and $\delta V_P$ near −10%. But synthetics for these models do not have the multiple arrivals we observe in these data (Figure S52). We note that for the other events shown here (Figures 4g and 4h), the waveforms are not as distinctive and can be fit equally well by a larger number models but that these events are also well explained by models with $\delta V_S$ and $\delta V_P$ near −40% and −10%, respectively. These models all cluster around $\delta V_S = -40\%$, $\delta V_P = -10\%$, thickness = 30 km, length along CMB = 4.0° (~250 km), and distance from source = 12°. Synthetics are shown overlain on data stacks in Figures 4b and 4d. Variation in $\delta V_S$ and $\delta V_P$ of ±5% also provides acceptable data misfit. Variations of either $\delta V_S$ or $\delta V_P$ by as much as

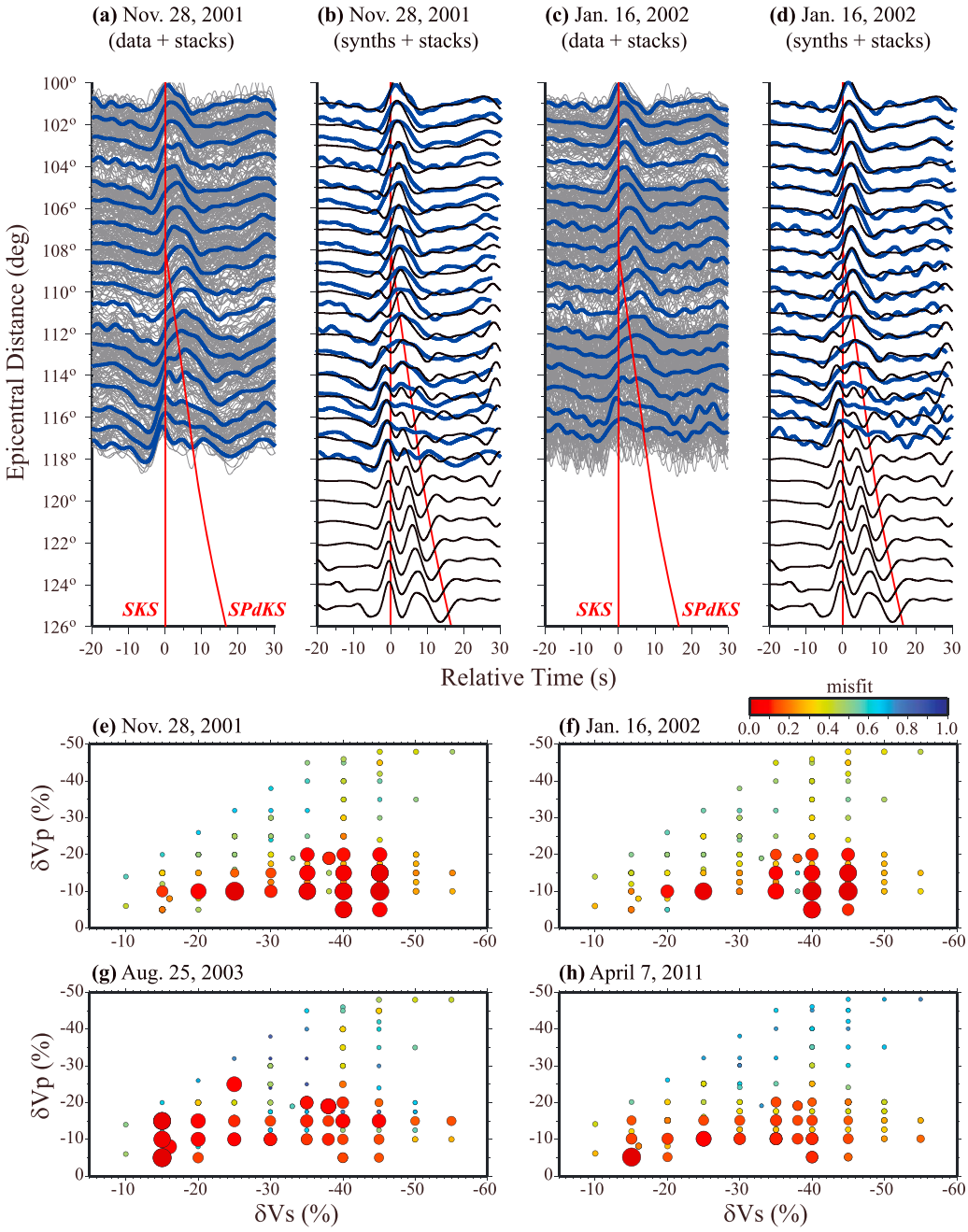


**Figure 4.** . (a and c) Radial component; displacement seismograms are shown in gray for data recorded by the Hi-net array in Japan for events occurring on 28 November 2001 (14:32) and 16 January 2002 (23:09). Blue traces show data stacks in 1° epicentral distance bins. PREM predicted *SPdKS* arrival times are shown with respect to *SKS* in red. (b and d) Data stacks (blue) are overlain on synthetic predictions (black) for a ULVZ model with the following parameters: $\delta V_S = -40\%$, $\delta V_P = -10\%$, $\delta\rho = +10\%$, thickness = 30 km, length in great circle arc direction = 4°, and the ULVZ edge located at 12° from the source. (e–h) Model misfit as a function of *S* and *P* wave velocity reduction for four events sampling the northern Mexico ULVZ. Root-mean-square misfit is normalized between 0 and 1 for each event. Circle size is scaled such that the lowest misfits have the largest circle sizes. ULVZ = ultralow-velocity zone.

10% with respect to the −40% and −10% optimum values significantly changes the timing between arrivals. No models are found with thickness less than 20 km that fit the character of these data.

The complex seismic waveforms recorded in this region are related to the interference of secondary phases with the *SPdKS* arrival. Most notable are arrivals generated when the down going *S* wave interacts with the

ULVZ. When the *S* wave reaches the edges of a ULVZ *P* wave energy is created, which travels at Pd moveout (Movie S1). A negative polarity arrival is generated at the leading edge of the ULVZ and a positive polarity arrival is generated at the far edge of the ULVZ. Both arrivals have travel time moveouts similar to *SPdKS*. These arrivals can lead to destructive and constructive interference with *SPdKS*.

## 5. Discussion and Conclusions

The ULVZ models providing the best fit to data analyzed in this study cluster around $\delta V_S = -40\%$ and $\delta V_P = -10\%$. However, several factors may affect our results that were not included in our modeling. (1) This region contains a D″ discontinuity (Thomas et al., 2004; Whittaker et al., 2016). Embedding ULVZs within a D″ layer may introduce additional waveform subtleties. However, this primarily introduces small-amplitude variations (see Figure S50). (2) The presence of slabs and slab debris can introduce additional waveform artifacts (Sun et al., 2016; Zhan et al., 2014). We have possible complications from slabs on the source and receiver sides. However, similarly shaped anomalous waveforms are observed for paths leaving the Central American slab at a wide variety of azimuths and are also recorded at stations far from the slabs subducting beneath Japan (Figures S2–S43). Hence, it appears unlikely that the anomalous waveforms we observe result from slab structure. (3) We only consider box-car-shaped ULVZs in 2-D. Variations in 2-D ULVZ shape alter waveform characteristics (Vanacore et al., 2016), and it is expected that 3-D ULVZ shapes will as well. Computing high-frequency synthetic seismograms for 3-D models is currently possible, albeit at high computational cost (Leng et al., 2016), and will be important in future efforts.

One previous study concluded that a ULVZ likely exists beneath Mexico using postcursors to *PcP* arrivals (Havens & Revenaugh, 2001). This study inferred a ULVZ with dimensions at least 300 km × 500 km on the CMB. Their preferred model has *P* and *S* wave velocity reductions from 7–8% and 14–16%, respectively, with a 14–16% increase in density and a thickness from 15 to 20 km. This study also identified a zone on the eastern side of this ULVZ that the authors were hesitant to interpret. Havens and Revenaugh (2001) suggested this zone could be one of the most anomalous ULVZ regions on Earth with a thickness of up to 40 km and *S* wave velocity reductions as large as 45%; findings similar to our study.

Compositional anomalies are consistent with observed *P* and *S* wave velocities associated with ULVZs (Brown et al., 2015; Sun et al., 2013; Wicks et al., 2017). In particular, mixtures of iron enriched (Mg,Fe)O and (Mg,Fe)$SiO_3$ may be able to produce the velocities we observe in this study. Although a compositional ULVZ is not out of the question, these studies suggest a *P* wave velocity decrease in excess of the 10–15% decrease observed here would be required. Thus, we suggest that these ULVZs contain some amount of partial melt. Several scenarios exist that may explain the occurrence of partial melt here. A thin layer of partial melt or discrete pockets of partial melt may have already existed at the CMB prior to the slabs arrival to the CMB (Labrosse et al., 2007). As the downgoing slab reaches the CMB it may push the partially molten material to the side creating the pockets of ULVZs. Geodynamic simulations (Tan et al., 2002) suggest that under the right conditions, downgoing slabs can induce upwelling material near the slab boundary and possibly produce melt through decompression melting. Another possibility is that the slab, once sitting atop the CMB, acts as a thermal blanket trapping heat. Over time the temperature beneath the slab increases to the point where melting starts to occur. A final scenario is that MORB in the slab starts to melt. MORB is expected to have the lowest melting temperature of lower mantle constituents and hydrated MORB could melt at even lower temperatures (Andrault et al., 2014).

If MORB is melting, then reactions with Fe-bearing minerals in the surrounding mantle are expected to suck in Fe, potentially making a dense melt sitting atop the CMB (Pradhan et al., 2015). This melt could get swept away toward LLSVPs (Li et al., 2017). Partially molten ULVZs could get refreshed as MORB continues to melt during the slab's descent. It is unclear whether these ULVZs would remain partially molten or evolve into compositional anomalies (Andrault et al., 2014). The partial melt could be enriched in FeO (Pradhan et al., 2015), commensurate with inferences of highly Fe-enriched FeO compositional ULVZs (Brown et al., 2015). If ULVZs are generated by melting of MORB, then additional partially molten ULVZs should also be detected in the vicinity of downwelling's. Future efforts should continue to search for ULVZs near the borders of high wave speed regions in tomographic models as the origin of ULVZs could lie there.

**Acknowledgments**

IRIS data were collected using the SOD utility (Owens et al., 2004). F-net and Hi-net recordings were obtained from the NIED. We acknowledge the University of Utah Center for High Performance Computing for computer resources and support. Figures were drawn using the Generic Mapping Tools (Wessel & Smith, 1998). Data analysis utilized SACTOOLS (Thorne, 2018). M. T. was partially supported through the Earthquake Research Institute (ERI) at the University of Tokyo and NSF grants EAR-1401097 and EAR-1723081. N. T. was partially supported by JSPS KAKENHI Grants JP15H05832 and JP18K03798. This manuscript benefitted from review by Don Helmberger, Dan Frost, the Associate Editor, and Editor Jeroen Ritsema. Data used are available at http://home.chpc.utah.edu/~thorne/data.html website.

## References

Andrault, D., Pesce, G., Bouhifd, M. A., Bolfan-Casanova, N., Hénot, J.-M., & Mezouar, M. (2014). Melting of subducted basalt at the core-mantle boundary. *Science*, *344*(6186), 892–895. https://doi.org/10.1126/science.1250466

Anzellini, S., Dewaele, A., Mezouar, M., Loubeyre, P., & Morard, G. (2013). Melting of iron at Earth's inner core boundary based on fast X-ray diffraction. *Science*, *340*(6131), 464–466. https://doi.org/10.1126/science.1233514

Avants, M., Lay, T., & Garnero, E. J. (2006). A new probe of ULVZ *S*-wave velocity structure: Array stacking of ScS waveforms. *Geophysical Research Letters*, *33*, L07314. https://doi.org/10.1029/2005GL024989

Berryman, J. G. (2000). Seismic velocity decrement ratios for regions of partial melt in the lower mantle. *Geophysical Research Letters*, *27*(3), 421–424. https://doi.org/10.1029/1999GL008402

Boschi, L., Becker, T. W., & Steinberger, B. (2007). Mantle plumes: Dynamic models and seismic images. *Geochemistry Geophysics Geosystems*, *8*, Q10006. https://doi.org/10.1029/2007GC001733

Bower, D. J., Wicks, J. K., Gurnis, M., & Jackson, J. M. (2011). A geodynamic and mineral physics model of a solid-state ultralow-velocity zone. *Earth and Planetary Science Letters*, *303*(3-4), 193–202. https://doi.org/10.1016/j.epsl.2010.12.035

Brown, S. P., Thorne, M. S., Miyagi, L., & Rost, S. (2015). A compositional origin to ultralow-velocity zones. *Geophysical Research Letters*, *42*, 1039–1045. https://doi.org/10.1002/2014GL062097

Cottaar, S., & Romanowicz, B. (2012). An unusually large ULVZ at the base of the mantle near Hawaii. *Earth and Planetary Science Letters*, *355-356*, 213–222. https://doi.org/10.1016/j.epsl.2012.09.005

Dziewonski, A. M., & Anderson, D. L. (1981). Preliminary reference Earth model. *Physics of the Earth and Planetary Interiors*, *25*, 297–356.

French, S. W., & Romanowicz, B. (2015). Broad plumes rooted at the base of the Earth's mantle beneath major hotspots. *Nature*, *525*(7567), 95–99. https://doi.org/10.1038/nature14876

Fukao, Y., Widiyantoro, S., & Obayashi, M. (2001). Stagnant slabs in the upper and lower mantle transition region. *Reviews of Geophysics*, *39*(3), 291–323. https://doi.org/10.1029/1999RG000068

Garnero, E. J., Grand, S. P., & Helmberger, D. V. (1993). Low *P*-wave velocity at the base of the mantle. *Geophysical Research Letters*, *20*(17), 1843–1846. https://doi.org/10.1029/93GL02009

Garnero, E. J., & Helmberger, D. V. (1998). Further structural constraints and uncertainties of a thin laterally varying ultralow-velocity layer at the base of the mantle. *Journal of Geophysical Research*, *103*(B6), 12,495–12,509.

Grand, S. P. (2002). Mantle shear-wave tomography and the fate of subducted slabs. *Philosophical Transactions of the Royal Society London A*, *360*(1800), 2475–2491. https://doi.org/10.1098/rsta.2002.1077

Grand, S. P., van der Hilst, R. D., & Widiyantoro, S. (1997). Global seismic tomography: A snapshot of convection in the Earth. *GSA Today*, *7*(4), 1–7.

Havens, E., & Revenaugh, J. (2001). A broadband seismic study of the lowermost mantle beneath Mexico: Constraints on ultralow velocity zone elasticity and density. *Journal of Geophysical Research*, *106*(B12), 30,809–30,820. https://doi.org/10.1029/2000JB000072

Helmberger, D. V., Ni, S., Wen, L., & Ritsema, J. (2000). Seismic evidence for ultralow-velocity zones beneath Africa and eastern Atlantic. *Journal of Geophysical Research*, *105*(B10), 23,865–23,878. https://doi.org/10.1029/2000JB900143

Helmberger, D. V., Wen, L., & Ding, X. (1998). Seismic evidence that the source of the Iceland hotspot lies at the core-mantle boundary. *Nature*, *396*(6708), 251–255. https://doi.org/10.1038/24357

Houser, C., Masters, G., Shearer, P., & Laske, G. (2008). Shear and compressional velocity models of the mantle from cluster analysis of long-period waveforms. *Geophysical Journal International*, *174*(1), 195–212. https://doi.org/10.1111/j.1365-246X.2008.03763.x

Hutko, A. R., Lay, T., & Revenaugh, J. (2009). Localized double-array stacking analysis of PcP: D″ and ULVZ structure beneath the Cocos plate, Mexico, central Pacific, and north Pacific. *Physics of the Earth and Planetary Interiors*, *173*(1-2), 60–74. https://doi.org/10.1016/j.pepi.2008.11.003

Idehara, K., Yamada, A., & Zhao, D. (2007). Seismological constraints on the ultralow velocity zones in the lowermost mantle from core-reflected waves. *Physics of the Earth and Planetary Interiors*, *165*(1-2), 25–46. https://doi.org/10.1016/j.pepi.2007.07.005

Jahnke, G. (2009). *Methods for seismic wave propagation on local and global scales with finite differences* (p. 99). München: Ludwig-Maximilians-Universität.

Jensen, K. J., Thorne, M. S., & Rost, S. (2013). *SPdKS* analysis of ultralow-velocity zones beneath the western Pacific. *Geophysical Research Letters*, *40*, 4574–4578. https://doi.org/10.1002/grl.50877

Labrosse, S., Hernlund, J. W., & Coltice, N. (2007). A crystallizing dense magma ocean at the base of the Earth's mantle. *Nature*, *450*(7171), 866–869. https://doi.org/10.1038/nature06355

Leng, K., Nissen-Meyer, T., & van Driel, M. (2016). Efficient global wave propagation adapted to 3-D structural complexity: A pseudospectral/spectral-element approach. *Geophysical Journal International*, *207*(3), 1700–1721. https://doi.org/10.1093/gji/ggw363

Li, M., McNamara, A. K., Garnero, E. J., & Yu, S. (2017). Compositionally-distinct ultra-low velocity zones on Earth's core-mantle boundary. *Nature Communications*, *8*(1), 177–179. https://doi.org/10.1038/s41467-017-00219-x

McNamara, A. K., Garnero, E. J., & Rost, S. (2010). Tracking deep mantle reservoirs with ultra-low velocity zones. *Earth and Planetary Science Letters*, *299*(1-2), 1–9. https://doi.org/10.1016/j.epsl.2010.07.042

Ni, S., & Helmberger, D. V. (2001). Probing an ultra-low velocity zone at the core mantle boundary with *P* and *S* waves. *Geophysical Research Letters*, *28*(12), 2345–2348. https://doi.org/10.1029/2000GL012766

Niu, F., & Wen, L. (2001). Strong seismic scatterers near the core-mantle boundary west of Mexico. *Geophysical Research Letters*, *28*(18), 3557–3560.

Owens, T. J., Crotwell, H. P., Groves, C., & Oliver-Paul, P. (2004). SOD: Standing order for data. *Seismological Research Letters*, *75*(4), 515–520. https://doi.org/10.1785/gssrl.75.4.515-a

Pradhan, G. K., Fiquet, G., Siebert, J., Auzende, A.-L., Morard, G., Antonangeli, D., & Garbarino, G. (2015). Melting of MORB at core-mantle boundary. *Earth and Planetary Science Letters*, *431*, 247–255. https://doi.org/10.1016/j.epsl.2015.09.034

Reasoner, C., & Revenaugh, J. (2000). *ScP* constraints on ultralow-velocity zone density and gradient thickness beneath the Pacific. *Journal of Geophysical Research*, *105*(B12), 28,173–28,182. https://doi.org/10.1029/2000JB900331

Ritsema, J., Deuss, A., van Heijst, H.-J., & Woodhouse, J. H. (2011). S40RTS: A degree-40 shear-velocity model for the mantle from new Rayleigh wave dispersion, teleseismic traveltime and normal-mode splitting function measurements. *Geophysical Journal International*, *184*(3), 1223–1236. https://doi.org/10.1111/j.1365-246X.2010.04884.x

Rost, S., Garnero, E. J., & Stefan, W. (2010). Thin and intermittent ultralow-velocity zones. *Journal of Geophysical Research*, *115*, B06312. https://doi.org/10.1029/2009JB006981

Sigloch, K., & Mihalynuk, M. G. (2013). Intra-oceanic subduction shaped the assembly of Cordilleran North America. *Nature*, *496*(7443), 50–56. https://doi.org/10.1038/nature12019

Simmons, N. A., Forte, A. M., Boschi, L., & Grand, S. P. (2010). GyPSuM: A joint tomographic model of mantle density and seismic wave speeds. *Journal of Geophysical Research*, *115*, B12310. https://doi.org/10.1029/2010JB007631

Spica, Z., Perton, M., & Beroza, G. C. (2017). Lateral heterogeneity imaged by small-aperture ScS retrieval from the ambient seismic field. *Geophysical Research Letters*, *44*, 8276–8284. https://doi.org/10.1002/2017GL073230

Sun, D., Helmberger, D. V., Jackson, J. M., Clayton, R. W., & Bower, D. J. (2013). Rolling hills on the core-mantle boundary. *Earth and Planetary Science Letters*, *361*, 333–342. https://doi.org/10.1016/j.epsl.2012.10.027

Sun, D., Helmberger, D. V., Miller, M. S., & Jackson, J. M. (2016). Major disruption of D″ beneath Alaska. *Journal of Geophysical Research: Solid Earth*, *121*, 3534–3556. https://doi.org/10.1002/2015JB012534

Takeuchi, N. (2007). Whole mantle SH velocity model constrained by waveform inversion based on three-dimensional Born kernels. *Geophysical Journal International*, *169*(3), 1153–1163. https://doi.org/10.1111/j.1365-246X.2007.03405.x

Takeuchi, N., & Obara, K. (2010). Fine-scale topography of the D″ discontinuity and its correlation to volumetric velocity fluctuations. *Physics of the Earth and Planetary Interiors*, *183*(1-2), 126–135. https://doi.org/10.1016/j.pepi.2010.06.002

Tan, E., Gurnis, M., & Han, L. (2002). Slabs in the lower mantle and their modulation of plume formation. *Geochemistry, Geophysics, Geosystems*, *3*(11), 1067. https://doi.org/10.1029/2001GC000238

Thomas, C., Garnero, E. J., & Lay, T. (2004). High-resolution imaging of lowermost mantle structure under the Cocos plate. *Journal of Geophysical Research*, *109*, B08307. https://doi.org/10.1029/2004JB003013

Thorne, M. S. (2018), SACTOOLS v1.0.0, Zenodo, doi:https://doi.org/10.5281/zenodo.1314738.

Thorne, M. S., Garnero, E. J., & Grand, S. P. (2004). Geographic correlation between hot spots and deep mantle lateral shear-wave velocity gradients. *Physics of the Earth and Planetary Interiors*, *146*(1-2), 47–63. https://doi.org/10.1016/j.pepi.2003.09.026

Thorne, M. S., Garnero, E. J., Jahnke, G., Igel, H., & McNamara, A. K. (2013). Mega ultra low velocity zone and mantle flow. *Earth and Planetary Science Letters*, *364*, 59–67. https://doi.org/10.1016/j.epsl.2012.12.034

Tonegawa, T., Hirahara, K., Shibutani, T., & Shiomi, K. (2006). Upper mantle imaging beneath the Japan Islands by Hi-net tiltmeter recordings. *Earth Planets Space*, *58*(8), 1007–1012. https://doi.org/10.1186/BF03352605

Torsvik, T. H., Smethurst, M. A., Burke, K., & Steinberger, B. (2006). Large igneous provinces generated from the margins of the large low-velocity provinces in the deep mantle. *Geophysical Journal International*, *167*(3), 1447–1460. https://doi.org/10.1111/j.1365-246X.2006.03158.x

Vanacore, E. A., Rost, S., & Thorne, M. S. (2016). Ultralow-velocity zone geometries resolved by multidimensional waveform modeling. *Geophysical Journal International*, *206*(1), 659–674. https://doi.org/10.1093/gji/ggw114

Wen, L. (2000). Intense seismic scattering near the Earth's core-mantle boundary beneath the Comores hotspot. *Geophysical Research Letters*, *27*(22), 3627–3630. https://doi.org/10.1029/2000GL011831

Wen, L., & Helmberger, D. V. (1998). A two-dimensional P-SV hybrid method and its application to modeling localized structures near the core-mantle boundary. *Journal of Geophysical Research*, *103*(B8), 17,901–17,918. https://doi.org/10.1029/98JB01276

Wessel, P., & Smith, W. H. F. (1998). New, Improved version of generic mapping tools released. *Eos, Transactions, American Geophysical Union*, *79*(47), 579. https://doi.org/10.1029/98EO00426

Whittaker, S., Thorne, M. S., Schmerr, N. C., & Miyagi, L. (2016). Seismic array constraints on the D″ discontinuity beneath Central America. *Journal of Geophysical Research: Solid Earth*, *121*, 152–169. https://doi.org/10.1002/2015JB012392

Wicks, J., Jackson, J. M., Sturhahn, W., & Zhang, D. (2017). Sound velocity and density of magnesiowüstites: Implications for ultralow-velocity zone topography. *Geophysical Research Letters*, *44*, 2148–2158. https://doi.org/10.1002/2016GL071225

Williams, Q., & Garnero, E. J. (1996). Seismic evidence for partial melt at the base of Earth's mantle. *Science*, *273*(5281), 1528–1530. https://doi.org/10.1126/science.273.5281.1528

Williams, Q., Revenaugh, J., & Garnero, E. J. (1998). A correlation between ultra-low basal velocities in the mantle and hot spots. *Science*, *281*(5376), 546–549. https://doi.org/10.1126/science.281.5376.546

Yu, S., & Garnero, E. J. (2018). Ultralow velocity zone locations: A global assessment. *Geochemistry, Geophysics, Geosystems*, *19*, 396–414. https://doi.org/10.1002/2017GC007281

Yuan, K., & Romanowicz, B. (2017). Seismic evidence for partial melting at the root of major hot spot plumes. *Science*, *357*(6349), 393–397. https://doi.org/10.1126/science.aan0760

Zhan, Z., Helmberger, D. V., & Li, D. (2014). Imaging subducted slab structure beneath Sea of Okhotsk with teleseismic waveforms. *Physics of the Earth and Planetary Interiors*, *232*, 30–35. https://doi.org/10.1016/j.pepi.2014.03.008

Zhang, D., Jackson, J. M., Zhao, J., Sturhahn, W., Alp, E. E., Hu, M. Y., et al. (2016). Temperature of Earth's core constrained from melting of Fe and $Fe_{0.9}Ni_{0.1}$ at high pressures. *Earth and Planetary Science Letters*, *447*, 72–83. https://doi.org/10.1016/j.epsl.2016.04.026